Common physiological processes control mercury reduction during photosynthesis and fermentation

Running title: Isotopes unify bacterial controls on Hg reduction

Daniel S. Grégoire [a*#], Sarah E. Janssen [b], Noémie C. Lavoie [a], Michael T. Tate [b], & Alexandre J. Poulain [a]

a - Biology Department, University of Ottawa, 30 Marie Curie, Ottawa, ON, K1N 6N5, Canada.

b - Upper Midwest Water Science Center, USGS, Middleton, Wisconsin 53562, USA.

Corresponding author: Dr. Daniel S. Grégoire, daniel.gregoire@uwaterloo.ca

* Current affiliation: Biology Department, University of Waterloo, 200 University Ave W, Waterloo, ON, N2L 3G1

Word count for abstract: 248

Word count for text (excluding abstract and importance sections): 4968

ABSTRACT

Mercury (Hg) is a global pollutant and potent neurotoxin that bioaccumulates in food webs as monomethylmercury (MeHg). The production of MeHg is driven by anaerobic and Hg redox cycling pathways such as Hg reduction, which control the availability of Hg to methylators. Anaerobes play an important role in Hg reduction in methylation hotspots, yet their contributions remain underappreciated due to how challenging these pathways are to study in the absence of dedicated genetic targets and low levels of Hg^0 in anoxic environments. In this study we used Hg stable isotope fractionation to explore Hg reduction during anoxygenic photosynthesis and fermentation in the model anaerobe *Heliobacterium modesticaldum* Ice1. We show that cells preferentially reduce lighter Hg isotopes in both metabolisms leading to mass-dependent fractionation, but mass-independent fractionation commonly induced by UV-visible light is absent. We show that isotope fractionation is affected by the interplay between pathways controlling Hg recruitment, accessibility, and availability alongside metabolic redox reactions. The combined contributions of these processes lead to isotopic enrichment during anoxygenic photosynthesis that is in between the values reported for anaerobic respiratory microbial Hg reduction and abiotic photoreduction. Isotope enrichment during fermentation is closer to what has been observed in aerobic bacteria that reduce Hg through dedicated detoxification pathways. These results demonstrate that common controls exist at the atomic level for Hg reduction during photosynthesis and fermentation in *H. modesticaldum*. Our work suggests that similar controls likely underpin diverse microbe-mediated Hg transformations that affect Hg's fate in oxic and anoxic habitats.

IMPORTANCE

Anaerobic and photosynthetic bacteria that reduce mercury affect mercury delivery to microbes in methylation sites that drive bioaccumulation in food webs. Anaerobic mercury reduction pathways remain underappreciated in the current view of the global mercury cycle because they are challenging to study, bearing no dedicated genetic targets to establish physiological mechanisms. In this study we used stable isotopes to show that common physiological processes control mercury reduction during photosynthesis and fermentation in the model anaerobe *Heliobacterium modesticaldum* Ice1. The sensitivity of isotope analyses highlighted the subtle contribution of mercury uptake towards the isotope signature associated with anaerobic mercury reduction. When considered alongside the isotope signatures associated with microbial pathways for which genetic determinants have been identified, our findings underscore the narrow range of isotope enrichment that is characteristic of microbial mercury transformations. This suggests that there exist common atomic-level controls for biological mercury transformations across a broad range of geochemical conditions.

59 **INTRODUCTION**

60 Mercury (Hg) is a global pollutant and potent neurotoxin that bioaccumulates in aquatic and
61 terrestrial food webs as monomethylmercury (MeHg) (1). Anaerobic microbes with the *hgcAB*
62 gene cluster, which encodes for the metabolic machinery responsible for Hg methylation (2),
63 contribute to MeHg production in habitats such as aquatic sediments, water columns, and
64 flooded soils (3-6). Hg methylation is thought to occur intracellularly and as such, it is ultimately
65 controlled by the bioavailability of Hg to methylators in anoxic habitats (7).

66 Hg redox cycling plays a key role in determining the inorganic Hg substrates available to
67 methylators. Its role is two-fold: anaerobic Hg^0 oxidation can supply dissolved Hg^{II} required to
68 generate MeHg and evasion of Hg^0 due to reduction can limit MeHg production by removing
69 inorganic Hg substrates. Although it is well established that abiotic photochemical Hg reduction
70 dominates Hg redox cycling in oxic surface systems where light is present (8-16), Hg reduction
71 pathways in anoxic zones where Hg methylation occurs have mostly been characterized under
72 laboratory conditions and remain challenging to assess in the field.

73 Anoxic Hg reduction can occur via abiotic redox reactions with dissolved organic carbon
74 (17) and magnetite (18, 19), but also through biotic pathways mediated by chemotrophic and
75 phototrophic microorganisms (20-24). Unlike many aerobes that reduce Hg using dedicated
76 enzymatic machinery encoded by the *mer* operon (25, 26), Hg reduction in anaerobes occurs
77 through cometabolic pathways tied to anaerobic respiration, fermentation, and anoxygenic
78 photosynthesis (20-24). In contrast to *mer*-mediated Hg reduction and demethylation, dedicated
79 genetic determinants have yet to be identified for anaerobic Hg reduction, making these
80 pathways challenging to study from a mechanistic standpoint. Furthermore, while some studies
81 have shown that Hg^0 can significantly contribute to Hg speciation in anoxic habitats (27, 28), it is

82 possible that low levels of Hg^0 are maintained by an active cycle of reduction and oxidation (29).
83 In the absence of genetic targets and measurable Hg^0 accumulation, the contributions of
84 anaerobic Hg^0 production to global Hg cycling remain cryptic and difficult to assess.
85 The use of stable Hg isotope fractionation is a powerful tool for providing
86 biogeochemical proxies for different abiotic and biotic Hg transformations (30, 31). All abiotic
87 and biotic Hg transformation pathways studied to date demonstrate kinetic mass dependent
88 fractionation (MDF) in which the product pool becomes isotopically lighter (enrichment of light
89 isotopes) as the reaction proceeds (32). Some pathways, such as abiotic photochemical reduction
90 and demethylation, also demonstrate mass independent fractionation (MIF), which is defined as
91 the fractionation that occurs outside of the predicted MDF pattern (30). MIF is most commonly
92 observed due to the magnetic isotope effect for odd-Hg isotopes ^{199}Hg and ^{201}Hg in the presence
93 of sunlight (33) and the extent to which MIF occurs is controlled in part by water chemistry and
94 the presence of photosynthetic organisms (39).
95 The combination of MDF and MIF tracers, and the rate of isotopic enrichment, referred
96 to as fractionation factor, can be used to outline the underlying components of different Hg
97 microbe-mediated Hg transformation pathways. Over the last decade, Hg isotope fractionation
98 has been studied in microbes capable of *mer*-mediated reduction (34) and MeHg demethylation
99 (35); anaerobic non-*mer*-mediated Hg reduction (36, 37); Hg methylation (37-40); and oxygenic
100 phototrophic MeHg degradation and Hg reduction (41). These studies have yielded valuable
101 insights and mechanistic details that explain how microbes interact with Hg at the atomic level
102 making them a promising option for studying mechanisms for anaerobic Hg reduction.
103

104 Our objective in this study was to characterize Hg isotope fractionation patterns during
105 anoxygenic phototrophic and fermentative Hg^{II} reduction, for which there exists no data. By
106 providing the first isotopic characterization of these pathways we aim to better understand the
107 underlying physiological pathways involved in anaerobic Hg reduction and their role in
108 controlling Hg availability to methylators in anoxic habitats. In this work, we test whether Hg
109 reduction by the model anaerobe *Heliobacterium modesticaldum* Ice1 during anoxygenic
110 photosynthesis and fermentation leads to distinct isotope enrichment signatures, which would
111 suggest the different metabolic Hg reduction pathways are controlled by separate processes. We
112 also compare our results to previously published isotope signatures for biotic and abiotic Hg
113 transformations to critically evaluate whether common controls exist for microbe-mediated Hg
114 transformations. Finally, we discuss whether current analytical capacity for isotope fractionation
115 can be used to track the contributions of such pathways in the environment.
116

117 # METHODS

118 **Cell growth conditions and bioreactor setup**

119 All experiments with live cells employed the strain *Heliobacterium modesticaldum* Ice1 grown
120 in PYE medium. Phototrophic cultures were grown at a constant visible light intensity of 80
121 µmol photon m^{-2} s^{-1} with a peak irradiance in the near-red to red spectrum (600 nm to 700 nm) at
122 50°C whereas chemotrophic cultures were grown in the dark at 50°C in line with our previous
123 work (23). *H. modesticaldum* Ice1 was obtained from the DSMZ culture collection (catalogue
124 number DSM-792). The bioreactor methodology employed in these experiments was similar to
125 the one used in previous work (23) with the following modifications: the bioreactor was
126 periodically supplied with sterile nitrogen gas that passed through an activated carbon filter and a

127 0.2 µm pore size air filter at a flow rate of 0.25 L min^{-1} and two gold traps were connected in
128 series at the reactor outlet to capture Hg^0 (**Fig S1**).
129 The bioreactor was kept in an incubator set to 50°C. Phototrophic experiments were
130 performed using a 60 W incandescent light bulb with a visible light intensity being maintained at
131 20 µmol photon $m^{-2}s^{-1}$ and mirroring the irradiance of growth conditions. Chemotrophic
132 experiments were performed in the dark. Background Hg^0 was purged and removed from
133 reactors prior to phototrophically or chemotrophically-grown *H. modesticaldum* cells being
134 added as a 10 % (v/v) inoculum wherein an additional subsample was withdrawn to verify initial
135 cell density via O.D. 600 nm. For sterile treatments, no cells were added to the bioreactor and the
136 volume of growth medium was adjusted to ensure experiments were carried out at a working
137 volume of 500 mL. In all experiments, NIST 3133, a standard with known Hg isotopic
138 composition, was added to the bioreactor to approximately10 nM Hg final concentration.
139 Additional details on bioreactor setup are provided in **Supporting Methods**.

140

141 **Hg^0 measurements**

142 The bioreactor was bubbled periodically rather than continuously in contrast to previous work
143 because continuous bubbling led to fouling of gold traps and poor total Hg (THg) and isotope
144 recoveries. Subsamples were collected at designated timepoints by connecting dual gold traps to
145 the reactor, purging the reactor for 30 min to collect Hg^0. In the final 5 mins the reactor liquid
146 was sampled for Hg^{II} concentration, isotopic composition, and cell growth after which gas flow
147 was stopped. All gold traps were capped to prevent Hg^0 loss and aqueous samples were
148 conserved with 1% (v/v) trace element grade HCl at 4°C in the dark. Reactor washes were
149 performed following previously established protocols (23).

150 **Total Hg analyses and sample preparation for stable isotope measurements**

151 All samples for aqueous Hg analyses were oxidized with 10 % (v/v) bromine chloride (BrCl) in
152 line with previous work (40) and THg concentrations were determined by stannous chloride
153 reduction coupled to cold vapor atomic fluorescence spectrometry (42). During THg analysis,
154 duplicates and matrix standard spikes were analyzed every 10 samples; analyses showed less
155 than 10 % relative percent difference between duplicates and spike recoveries of 90-110%. The
156 detection limit was 0.2 pM.

157 Total Hg mass balances were calculated in line with previous work (23, 24) with
158 corrections to account for the mass of Hg removed for each subsample. For Hg^0 collected onto
159 gold traps, a thermal desorption system was used to liberate Hg^0 over a 40 min desorption cycle
160 which was then captured in 40% HNO_3:BrCl (3:1) oxidizing solution. An aliquot of the trapping
161 solution was subsequently analyzed for THg concentration following the protocol established in
162 previous work (43). Desorption efficiency during pre-concentration was tested by trapping a
163 NIST 3133 standard with each batch of samples, and recoveries for standard trapping were
164 101.27 ± 4.26 (n = 15). THg recoveries from bioreactor experiments were 94.90 ± 9.50 % (n=7)
165 (**Fig S2**).

166

167 **Hg stable isotope analyses**

168 Using the previously determined THg concentration, an aliquot of the trapping solution was
169 diluted with ultra-high purity water to an acid content < 10% H^+ and a THg concentration of 3.75
170 to 5.00 nM (44). A Neptune Plus multicollector-inductively coupled plasma mass spectrometer
171 (MC-ICP-MS) was used for Hg stable isotope ratio measurements. A concentration and matrix-
172 matched NIST 3133 Hg was used for standard sample bracketing (45). To achieve detection at

low Hg concentrations, Hg was reduced with stannous chloride in-line then introduced continuously into a custom designed gas liquid separator along with a thallium standard (NIST SRM 997, 195 nM in 3% HCl) for mass bias correction (44, 46). MC-ICP-MS instrument conditions and analytical expectations derived from previously published work and quality control metrics for Hg stable isotope analysis are provided in **Supporting Methods, Table S1** and **Table S2**.

Isotope calculations

Delta calculations followed the conventions set forth by others (45). This convention calls for mass dependent fractionation (MDF) to be expressed in terms of δ^{xxx}Hg where graphically δ^{202}Hg is used to signify MDF. δ^{xxx}Hg is calculated as:

$$\delta^{xxx}\text{Hg}(‰) = [(^{xxx}\text{Hg}/^{198}\text{Hg}_{sample})/(^{xxx}\text{Hg}/^{198}\text{Hg}_{NIST\text{-}3133}) - 1] \times 1000. \quad (\textbf{Eq 1})$$

XXX is used to signify the isotope of interest. Hg also undergoes MIF of both even and odd isotopes. Here, odd-MIF is described by Δ^{199}Hg and even-MIF by Δ^{200}Hg. MIF is calculated as:

$$\Delta^{xxx}\text{Hg} \approx \delta^{xxx}\text{Hg} - (\delta^{202}\text{Hg} * \beta). \quad (\textbf{Eq 2})$$

β denotes the mass dependent scaling constant, which is determined by the laws of mass dependence (45). Isotope enrichment effects based on the ratio of products to reactants (i.e. $\varepsilon_{p/r}$, herein referred to as ε_{AP} for anoxygenic phototrophic reduction and ε_{FM} for fermentative reduction) were calculated using Rayleigh fractionation models to account for the Hg^0 that was removed following methods from previous work on microbial Hg reduction (34).

This method involved fitting a linear regression (shown in **Fig S3, Fig S4,** and **Table S3**) based on the change in relative isotope ratios, ln (R/R_0), as a function of ln(f_r) where:

$R = (\delta^{202}Hg/1000) + 1$ for Hg^{II} (reactant) or Hg^0 (product) at a given time point and

$R_0 = (\delta^{202}Hg/1000) + 1$ at the beginning of the experiment (**Eq 3**);

f_r= Hg^{II} in the reactor at a given time / Hg^{II} in the reactor at the start of the experiment (**Eq 4**); and the slope of the linear regression, which is equivalent to ε_{AP} or ε_{FM}:

$$\varepsilon = \ln (R/R_0)/ \ln(f_r) \quad \textbf{(Eq 5)}.$$

We chose to use the total Hg analyses from the bioreactor to establish f_r as this is a true representation of the instantaneous isotope fractionation rather than a time integrated sample following the methods outlined in previous work (34). Note that in our slope calculations we do not have data for $^{202}Hg^0$ when f_r=1 (the 0h sampling point) because no isotope fractionation was taking place prior to the start of Hg reduction (**Table S2** and **Table S3**). Additional calculations for isotope mass balances were carried out to test for deviation from the Rayleigh fraction model and can be found in **Table S4.** ε values for MDF were compiled from previous studies on pure microbial cultures and abiotic Hg transformations for comparison purposes. Currently, there is no standard guideline for how to calculate ε and studies vary widely in how they present isotope enrichment data and their associated variability. We have provided details on how we normalized ε values from different studies in **Table S5**. In this work we only compared enrichment factors from studies that used MC-ICP-MS techniques that were in line with our analyses, however we have included all of the enrichment factors for microbe-driven Hg transformations published to date in **Table S5**.

217 **RESULTS AND DISCUSSION**

218 **Hg^0 production during anoxygenic photosynthesis and fermentation**

219 In our experiments Hg^0 production relied on the presence of live cells for both chemotrophic and
220 phototrophic growth conditions. Cumulative Hg^0 production was an order of magnitude higher
221 for live cell treatments compared to abiotic controls (>0.60 vs <0.05 nmol) (**Fig 1**).
222 Chemotrophic cells produced double the amount of Hg^0 compared to phototrophic cells (1.33 to
223 1.64 nmol vs 0.60 to 0.81 nmol, respectively) despite having been supplied with slightly less Hg^{II}
224 (**Fig 1B, E**). In relative terms, phototrophic cells reduced 12 to 15% of the initial Hg^{II} supplied
225 whereas chemotrophic cells reduced 31 to 40% (**Fig S2**).

226 Relative Hg^0 production in these experiments was lower, yet consistent with our previous
227 work, which showed chemotrophically-grown cells reduced 15% more Hg^{II} than
228 phototrophically-grown cells, reducing between 60 to 75% of the initial Hg^{II} supplied (23). The
229 relative amount of Hg^0 production did not increase with higher Hg^{II} exposure (10 nM) versus
230 previous experiments (250 pM) (23). It is unlikely that the lower reduction rate observed in the
231 experiments presented here was due to the toxicity of 10 nM Hg supplied, given that *H.*
232 *modesticaldum* grows well under the same conditions at 50 times higher Hg concentrations (23).
233 Instead, we suspect that the lack of constant bubbling of the reactor may be responsible for the
234 observed results. It is possible that the accumulation of CO_2 in the bioreactor following organic
235 carbon oxidation may compete with Hg^{II} as an electron sink, decreasing the amount of Hg^0
236 produced. Inorganic carbon is required for anaplerotic reactions that fulfill the biosynthetic needs
237 of *H. modesticaldum* and CO_2 could have competed with Hg^{II} for reducing power, as previously
238 shown (47). These results could also be due to Hg^0 oxidation allowed by the increased residence

239 time of Hg^0 in the reactor afforded by the intermittent sparging, as has been observed in other

240 anaerobes (48, 49).

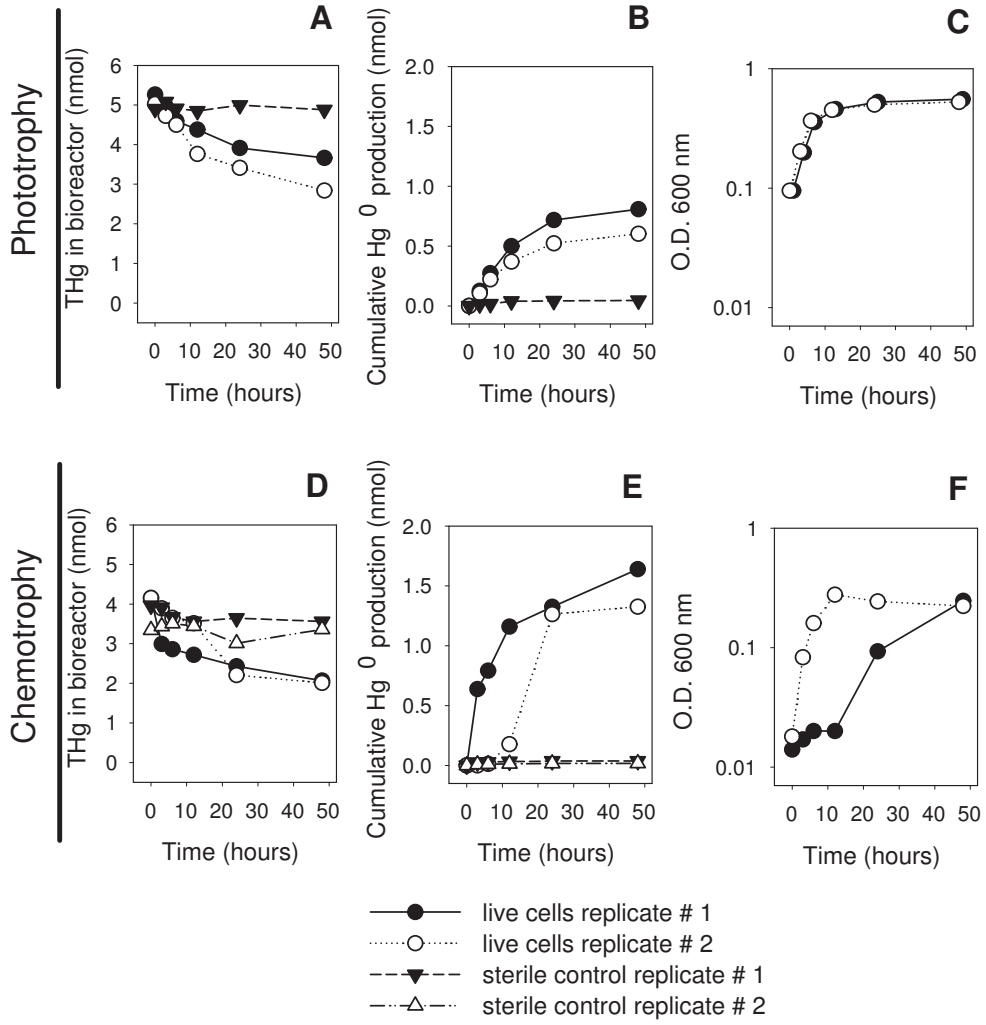

241

242 **Figure 1: Total Hg and cumulative Hg^0 production by *H. modesticaldum* grown**
243 **phototrophically and chemotrophically. A, D** THg for live cells and sterile controls without
244 cells. **B, E** Cumulative Hg^0 production for live cells and sterile controls without cells. **C, F**
245 Microbial growth as measured by O.D. 600 nm for live cells and sterile controls without cells. 10
246 nM Hg was supplied in all experiments from the same stock (NIST 3133).
247

248

249 Despite carefully controlling the growth conditions in our experiments, chemotrophic
250 cells from replicate #1 exhibited a lag phase of 12 hours (**Fig 1F**). Although this lag did not
251 affect final cell density, the slow-growing culture from replicate #1 initiated Hg^0 production
252 earlier than the culture in replicate #2 (**Fig 1E, F**). These results may be attributable to cells in
253 replicate #1 maintaining a higher Hg to cell ratio in the first 12 hours of the experiment, which
254 suggests that Hg is being reduced intracellularly in line with our previous work on Heliobacteria
255 (23, 50). Indeed, even at low initial densities, cells can maintain μM levels of intracellular
256 reducing power, which could be used to reduce nM levels of Hg^{II} (24).
257
258 **Mass dependent fractionation during photosynthetic and fermentative growth**
259 Hg reduction in phototrophically grown *H. modesticaldum* resulted in consistent positive MDF
260 whereas fermentatively grown cultures showed positive MDF with variability in fractionation
261 patterns across replicates (**Fig 2**). Abiotic controls showed minimal fractionation for both MDF
262 and MIF, confirming that Hg reduction and subsequent isotopic fractionation were
263 predominantly driven by cellular processes (**Fig 2**). Live cell experiments were devoid of MIF
264 (**Table S1** and **Table S2**).
265 For phototrophically-grown cultures, the reactant pool $\delta^{202}Hg^{II}$ increased steadily over time
266 suggesting cells preferentially reduced lighter Hg^{II} (**Fig 2A**). A mirror trend was observed for
267 $\delta^{202}Hg^0$, which was depleted in $^{202}Hg^0$ at the beginning of the experiment, became enriched with
268 heavier isotopes as the reaction proceeded, and eventually approached the initial isotopic
269 composition of the NIST 3133 standard (0‰) (**Fig 2B**).
270
271

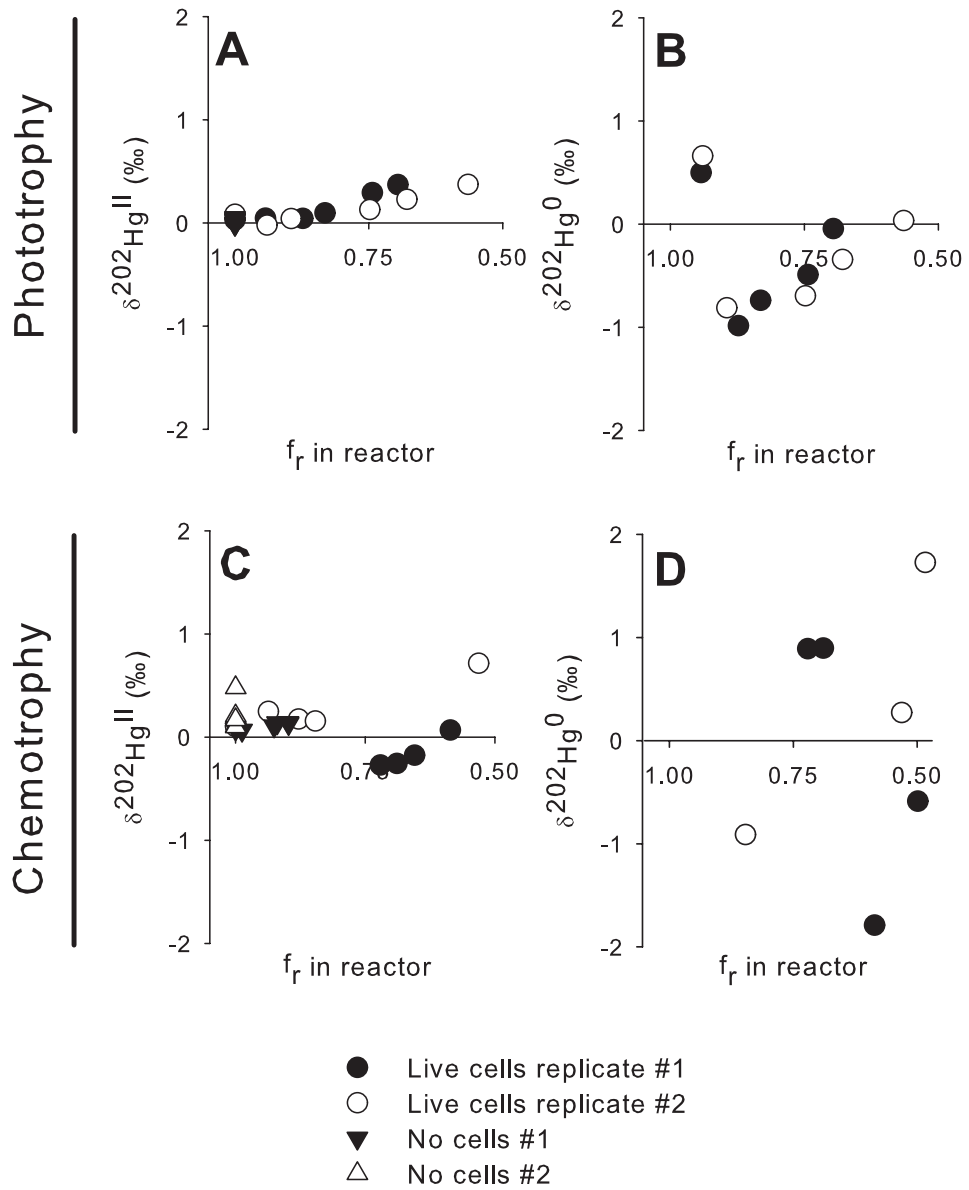

Figure 2: Mass dependent fractionation of ^{202}Hg in Hg^{II} (A, C) and Hg^{0} (B, D) during phototrophic and chemotrophic growth of *H. modesticaldum* and no cell controls. $\delta^{202}Hg$ values for Hg^{II} and Hg^{0} are plotted with respect to the fraction of remaining total inorganic Hg^{II} in the bioreactor. Insufficient Hg^{0} was recovered from the no cell controls and thus no results are displayed. 10 nM Hg was used in all experiments and Hg was supplied from the same stock (NIST 3133).

279 Curiously, the $\delta^{202}Hg^0$ for f_r = 0.94 at 3h in the two phototrophic live cell replicates showed
280 that the product pool was initially enriched with the $^{202}Hg^0$ isotope (**Fig 2B**). A similar pattern
281 has been observed in iron reducing bacteria that preferentially reduced heavier Fe^{III} (51) and the
282 model anaerobic Hg methylator and reducer *Geobacter sulfurreducens* PCA (37, 40). The most
283 recent work on *G. sulfurreducens* has shown that uptake of Hg selects for lighter Hg isotopes but
284 cells can also access an isotopically heavier pool of Hg^{II} from the dissolved phase (37). It is
285 possible that a similar process is occurring for phototrophically-grown *H. modesticaldum*
286 wherein cells access an isotopically heavier pool of Hg during equilibrium binding of Hg^{II} to the
287 outside of the cell, followed by an alternative uptake process that selects for lighter pools of Hg.
288 Based on these results, we included all time points in isotopic enrichment calculations for Hg^{II}
289 but omitted the 3h time point in calculations for Hg^0 given that other cellular fractionation
290 processes could be occurring (**Fig S3, Fig S4,** and **Table S3**).
291 Positive MDF was also observed for chemotrophic cultures but fractionation patterns differed
292 strongly between replicates. Replicate #1 showed an initial depletion in reactant pool $\delta^{202}Hg^{II}$ and
293 became progressively enriched with $^{202}Hg^{II}$ relative to the NIST 3133 suggesting lighter isotopes
294 were still preferentially reduced (**Fig 2C**). Note that the second $\delta^{202}Hg^{II}$ data point available for
295 replicate #1 occurs at f_r=0.72 due to the rapid rate of Hg^{II} reduction leading to substantially less
296 Hg remaining in the reactor (**Fig 1E** and **Fig 2C**). Results for replicate #2 further suggested that
297 lighter Hg^{II} isotopes were preferentially reduced with $\delta^{202}Hg^{II}$ slightly increasing at the
298 beginning of the experiment before rising to a maximum of 0.72 ‰ between f_r = 0.85 at 12h and
299 0.53 at 24h (**Fig 2C**).
300

The trends for $\delta^{202}Hg^0$ in chemotrophic cultures mirrored what was observed for $\delta^{202}Hg^{II}$. $\delta^{202}Hg^0$ from replicate #1 showed that the product pool was initially enriched with heavy $^{202}Hg^0$, further suggesting cells may have accessed a readily bioavailable pool of heavy Hg^{II}, before undergoing a pronounced depletion and progressive enrichment with heavy isotopes similar to phototrophic cultures (**Fig 2B, D**). In contrast, the $\delta^{202}Hg^0$ values for cells in replicate #2 suggest that the product pool was depleted in $^{202}Hg^0$ before undergoing enrichment for heavier Hg^0 isotopes reaching a maximum of 1.73 ‰ (**Fig 2D**).

The enrichment in $^{202}Hg^0$ exceeded the initial composition of the NIST 3133 standard (0 ‰) suggesting fractionation deviated from the predicted Rayleigh fractionation for Hg reduction (**Table S4**). Recent work with *G. sulfurreducens* has shown that subcellular partitioning processes contribute to Hg isotope fractionation and cannot be detected at the level of THg pool (37). In our work, Hg reduction provided such a strong isotopic shift that we could detect fractionation in the THg pool, however we cannot discount the contributions of subcellular partitioning processes, which are smaller in magnitude (<0.10 ‰). Such processes could be driving the depletion of $^{202}Hg^{II}$ early on for chemotrophic cells in replicate #1 where low cell densities may have amplified uptake and adsorption-driven fractionation (**Fig 1F**). It is more challenging to discuss contributions of such processes for replicate #2, where the low cumulative Hg^0 production at f_r = 0.94 and 0.88 (3h and 6h time points, respectively) precluded our ability to measure Hg^0 isotope fractionation (**Fig 1E** and **Table S2**). Despite this limitation, the high $\delta^{202}Hg^0$ value obtained for the final timepoint for replicate #2 reinforces that additional processes are contributing to fractionation under chemotrophic conditions that warrant further exploration.

Our experimental results suggest that Hg^0 oxidation is not a major contributor at earlier stages of reduction (i.e., 3-12 hours) but may be contributing to isotope fractionation at later time points associated with longer Hg residence times in the reactor. Under phototrophic conditions, the measured values of $\delta^{202}Hg^{II}$ at 48h were isotopically heavier than predicted values, which suggests Hg^0 oxidation may be occurring (**Table S4**). Under fermentative conditions the potential contribution of Hg oxidation is unclear, since a consistent enrichment was not observed between replicates (**Table S4**). The variability in isotope results for later time points in both replicates suggests processes other than reduction may be occurring.

Although Hg^0 oxidation has never been observed in anoxygenic phototrophs, it has been observed in other model chemotrophic anaerobes (49). Recent work showed that thiol-bearing molecules preferentially oxidize heavy $^{202}Hg^0$, leading to negative MDF, in addition to a MIF signal (52). Although we did not observe any negative MDF or MIF in our experiments (**Table S1** and **Table S2**), we acknowledge that such processes have the potential to contribute to net fractionation alongside internal partitioning related to uptake or adsorption processes. These results are an important first step to resolving the physiological processes that drive these Hg transformations in *H. modesticaldum* and we plan to carry out additional experiments to assess the contributions of uptake, adsorption, and redox transformations to the net Hg isotope fractionation observed in the future.

343 **Comparing enrichment factors for abiotic and biotic Hg transformations**

344 The average isotopic enrichment factor calculated using the ratio of product to reactant ($\varepsilon_{p/r}$) ± 2
345 standard deviations (2SD) for MDF in the reactant pool Hg^{II} during anoxygenic photosynthesis
346 (ε_{AP}) was -0.80 ± 0.56 ‰ whereas the average isotopic enrichment factor obtained during
347 fermentation (ε_{FM}) was -1.13 ± 0.50 ‰ (**Fig 3, Fig S3, Table S3,** and **Table S5**).

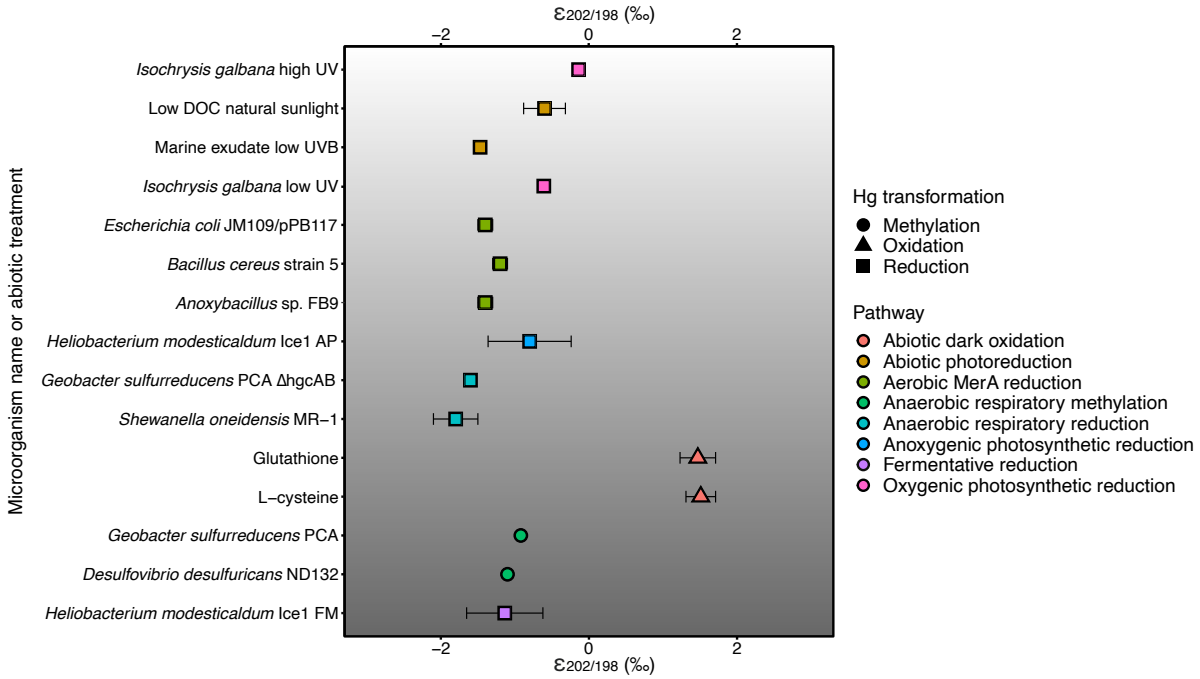

348

349 **Figure 3: Compilation of isotopic enrichment factors (ε) for abiotic and biotic Hg**
350 **transformations.** Hg transformations are denoted by different shapes and specific metabolic and
351 chemical pathways have been colour coded. Error bars denote 2 standard deviations for studies
352 where this data was available. In the event that data was presented as a standard error, standard
353 deviation was calculated based on the sample size indicated in each study. Abbreviations on the
354 y-axis denote the following: UV (ultraviolet light), DOC (dissolved organic carbon), AP
355 (anoxygenic photosynthesis), ΔhgcAB (no *hgcAB* gene cluster), and FM (fermentation). The
356 grey-shading in this figure represents light and oxygen. Lighter regions represent habitats where
357 light and oxygen are present and darker regions represent where they are not. The values in this
358 figure were obtained from the following studies: abiotic dark oxidation (52); abiotic
359 photoreduction (32, 41); aerobic MerA reduction (34, 36); anaerobic respiratory methylation
360 (40); anaerobic respiratory reduction (36, 37); anoxygenic photosynthetic reduction (this study);
361 fermentative reduction (this study); oxygenic photosynthetic reduction (41). The raw data in this
362 figure are in **Table S5**.

363 The enrichment factor could not be calculated using the product Hg^0 pool for fermentative
364 cultures and overestimated the value in phototrophic cultures (-2.86 ± 1.32 ‰) (**Fig S4** and
365 **Table S3**). Previous work has shown that using the product pool can overestimate the
366 fractionation factor due to difficulty obtaining analytical replicates of gaseous Hg^0 and the
367 complexity of quantitatively collecting this pool (53). As such, we carried out comparisons for
368 enrichment factors using the reactant Hg^{II} pool. Ideally, we would have been able to obtain more
369 replicates of our experiments but were unable to do so due the challenges stated previously. It is
370 important to note that low numbers of replicates are routinely discussed in isotope geochemistry
371 and the variability from our results is in line with previous work (**Fig 3** and **Table S5**).
372 Our initial motivation for this study was to test if phototrophic and fermentative Hg
373 reduction led to markedly different isotope enrichment factors and establish whether different
374 underlying processes supported different metabolic Hg reduction pathways. When comparing ε
375 values, which are used as an index to distinguish between different isotope fractionation
376 processes, we report a difference of 0.33 ‰ between ε_{AP} and ε_{FM} (**Fig 3** and **Table S5**). This
377 small difference in enrichment factors supports that common processes are controlling Hg
378 reduction during anoxygenic photosynthesis and fermentation in *H. modesticaldum*.
379 In our previous work with *H. modesticaldum* we demonstrated that inhibiting pyruvate
380 ferredoxin oxidoreductase, the enzyme responsible for the production of reduced ferredoxin,
381 greatly hampered Hg^{II} reduction during anoxygenic photosynthesis and fermentation (23). It is
382 possible that the similarity between ε_{AP} and ε_{FM} is the result of reactions originally involving the
383 same redox cofactors (e.g. ferredoxins) but with Hg^{II} being reduced by different electron donors
384 specific to each metabolism. Such reactions could involve direct electron transfer from
385 ferredoxin to Hg^{II} or from enzymes directly or indirectly relying on ferredoxin (23, 54). It is also

386 possible that the net isotopic enrichment stems from a combination of multiple processes
387 involved in Hg transport (e.g. adsorption, uptake, and efflux) that would occur regardless of the
388 intracellular transformations in question. Our results suggest that the relative contributions of
389 these processes may be more pronounced during fermentation compared to anoxygenic
390 photosynthesis although more controlled experiments are required to constrain the variability in
391 the isotope fractionation observed.

392 At the broader scale, the isotopic enrichment observed for both metabolisms tested in *H.*
393 *modesticaldum* falls between the values observed for abiotic and microbial Hg reduction
394 pathways (**Fig 3** and **Table S5**). The isotopic enrichment observed for phototrophic *H.*
395 *modesticaldum* is slightly lower than photoreduction in the presence of dissolved organic carbon
396 (-0.80 ± 0.56 ‰ vs -0.60 ± 0.20 ‰, respectively) (32) but higher than photoreduction in the
397 presence of marine exudates and UVB light (-0.80 ± 0.56 ‰ vs -1.47 ‰, respectively) (41) (**Fig**
398 **3** and **Table S5**). When comparing Hg reduction in the anoxygenic phototroph *H. modesticaldum*
399 to the oxygenic phototrophic green alga *Isochrysis galbana*, the isotopic enrichment observed is
400 also slightly lower (-0.80 ± 0.56 ‰ vs -0.14 to -0.60 ‰, respectively) (41) (**Fig 3** and **Table S5**).
401 Though this similarity suggests anoxygenic and oxygenic photosynthetic Hg reduction share a
402 common physiological pathway, the presence of MIF in *I. galbana* due to free radical generation
403 within the cell rules out this possibility (41). (**Table S1**). Thus, Hg reduction during anoxygenic
404 photosynthetic Hg reduction could be distinguished from other photo-induced reduction
405 pathways due to the lack of MIF tracer.
406

When compared with previous work on microbial Hg reduction in pure cultures, the isotopic enrichment observed for phototrophically-grown *H. modesticaldum* was higher than what has previously been reported for aerobic *mer*-mediated reduction and anaerobic respiratory Hg reduction (-0.80 ± 0.56 ‰ vs -1.80 to -1.20 ‰, respectively) (34, 36, 37) (**Fig 3** and **Table S5**). Interestingly, the isotopic enrichment observed in fermentatively-grown *H. modesticaldum* (-1.13 ± 0.50 ‰) was closer to aerobic *mer*-mediated reduction (-1.40 to -1.20 ‰) (34) than to anaerobic respiratory Hg reduction in *Shewanella oneidensis* MR-1 and a modified strain of *G. sulfurreducens* PCA incapable of Hg methylation (-1.80 to -1.60 ‰) (**Fig 3** and **Table S5**) (36, 37). An additional line of evidence supporting that Hg^0 oxidation is unlikely to be contributing to the isotope signature observed in our system are the ε values for thiol mediated Hg^0 oxidation in the dark. These values are considerably larger than what we observed for *H. modesticaldum* (1.51 ± 0.20 ‰ for cysteine and 1.47 ± 0.24 ‰ for glutathione) (**Fig 3** and **Table S5).**

These comparisons illustrate that isotopic enrichment for microbial Hg reduction pathways that only display MDF fall within a narrow range (i.e. -0.80 to -1.80 ‰) (**Fig 3** and **Table S5**). We find this to be a strikingly small difference given the ecological diversity of the model organisms and variety of growth conditions used to study microbial Hg reduction. The similar ε values reported for fermentation in this study and the *mer* operon are also noteworthy as they suggest nearly identical isotope enrichment can occur in aerobes harbouring dedicated enzymatic machinery to reduce Hg and anaerobes where *mer*-based strategies are largely absent.

Our study also shows that similar isotopic enrichment can be observed for different anaerobic Hg transformations. The anaerobic Hg methylating chemotrophs *G. sulfurreducens* PCA and *Desulfovibrio desulfuricans* ND132 displayed ε signatures (i.e. -0.92 and -1.1‰, respectively) that fall within the range of ε values we report in our study (i.e. -0.80 to -1.13 ‰)

430 (**Fig 3** and **Table S5**) (40). The similarity in enrichment signatures suggests that common
431 processes may affect the delivery of inorganic Hg substrates to intracellular sites independently
432 of the Hg transformations in question. Although it is outside of the scope of the current study,
433 identifying the nature of these processes may provide insights into similar controls that exist for
434 Hg uptake and transformation in anaerobes.

435 Our work showcases the strengths but also the challenges of using isotope fractionation-
436 based approaches to decipher cryptic Hg cycling pathways. To illustrate the challenges of using
437 isotopes to track Hg cycling pathways in the environment, we visualized our comparison of ε
438 values in the context of a vertically redox stratified habitat (e.g. a water column) (**Fig 3**).
439 Through Hg stable isotope fractionation, we can distinguish between abiotic and biotic redox
440 reaction pathways that control Hg's availability in methylation hotspots, such as the limit of the
441 photic zone, on the bases of MIF signatures associated with photochemical reactions. In contrast,
442 teasing apart biological pathways that contribute to the net isotope signature of Hg^{II} in the
443 environment is more challenging because competing MDF processes occur in both dark and
444 photo-mediated pathways where Hg^{II} is a reactant (e.g. reduction and methylation) and a product
445 (e.g. demethylation and oxidation). This overlap makes it difficult to translate δ^{202}Hg values
446 observed under controlled conditions that are sensitive to changes in cellular physiology to
447 environments where pools of bioavailable Hg are not homogenous due to variable mixing.
448

449 **CONCLUSION**

450 In this study we have provided the first evidence that common physiological processes drive
451 MDF during Hg reduction associated with anoxygenic photosynthesis and fermentation in the
452 model anaerobe *H. modesticaldum*. We show that isotopic enrichment during anoxygenic

453 phototrophic Hg reduction leads to an intermediate fractionation process that lies between
454 photochemical reactions and dark microbial Hg reduction. We also show that fermentative Hg
455 reduction leads to isotopic enrichment that is similar to aerobic *mer*-mediated reduction.
456 Although current analytical capacities to measure stable isotope fractionation make
457 applying such approaches to the environment challenging, this is a burgeoning field that has
458 advanced considerably in terms of sensitivity and the different Hg species that can be targeted in
459 the last 10 years. Isotope fractionation approaches have proved extremely valuable for teasing
460 apart the complex interwoven processes that drive microbe-mediated Hg transformations and as
461 seen in our study, highlighting common processes that control Hg bioavailability to microbes.
462 In future work, it will be important to isolate the different steps involved in Hg uptake
463 and transformation by rigorously controlling Hg availability and cellular physiology. Leveraging
464 molecular tools alongside isotopes will be a useful strategy to address these knowledge gaps and
465 the recent availability of genetically tractable *H. modesticaldum* deletion mutants offers a
466 promising means to do so (55). In that regard, gene deletion approaches targeting redox-active
467 enzymes could be used to characterize the physiological components contributing directly to Hg^{II}
468 reduction, whereas targeting homologues for proteins involved in Hg uptake in other model
469 anaerobes could be the key to identifying entry routes for Hg into *H. modesticaldum* (56, 57).
470 In addition to gene deletions, whole-genome, transcriptome, and proteome approaches
471 could be combined with isotopic analyses in pure cultures to hone in on potential biomarkers for
472 Hg transformation pathways that remain poorly understood. Such biomarkers could be used to
473 examine publicly available genomic datasets to assess the distribution of anaerobic Hg reducers
474 in modern day environments and rock records, the latter serving as an archive for Hg isotope
475 signatures and the microbial community involved in historical Hg cycling (31, 58). These ancient

environments were likely dominated by anoxygenic phototrophs that were important primary producers before the rise of oxygen on Earth. By using isotopes to create a window into the past, we can compare the selective forces that gave rise to fortuitous Hg reduction pathways tied to anaerobic metabolisms and dedicated detoxification strategies such as the *mer* operon.

ACKNOWLEDGMENTS

Our work was funded by NSERC Discovery and Accelerator grants, CFI funding to AJP and NSERC graduate scholarship to DSG. Instrumentation and lab operations for Hg isotope analyses were supported by the USGS Toxic Substances Hydrology Program. Any use of trade, firm, or product names is for descriptive purposes only and does not imply endorsement by the U.S. Government.

AUTHOR CONTRIBUTIONS

DSG, AJP, SEJ and MTT designed all experiments; DSG and NCL carried out bioreactor experiments and data analyses; SEJ and MTT carried out total Hg and stable isotope analyses; DSG, AJP, SEJ and MTT wrote the manuscript.

493 **REFERENCES**

494 1. Selin NE. 2009. Global biogeochemical cycling of mercury: A review. Annual Review of
495 Environment and Resources 34:43-63.

496 2. Parks JM, Johs A, Podar M, Bridou R, Hurt Jr RA, Smith SD, Tomanicek SJ, Qian Y,
497 Brown SD, Brandt CC, Palumbo AV, Smith JC, Wall JD, Elias DA, Liang L. 2013. The
498 genetic basis for bacterial mercury methylation. Science 339:1332-1335.

499 3. Fleming EJ, Mack EE, Green PG, Nelson DC. 2006. Mercury methylation from
500 unexpected sources: Molybdate-inhibited freshwater sediments and an iron-reducing
501 bacterium. Applied and Environmental Microbiology 72:457-464.

502 4. Han S, Narasingarao P, Obraztsova A, Gieskes J, Hartmann AC, Tebo BM, Allen EE,
503 Deheyn DD. 2010. Mercury speciation in marine sediments under sulfate-limited
504 conditions. Environmental Science and Technology 44:3752-3757.

505 5. Podar M, Gilmour CC, Brandt CC, Soren A, Brown SD, Crable BR, Palumbo AV,
506 Somenahally AC, Elias DA. 2015. Global prevalence and distribution of genes and
507 microorganisms involved in mercury methylation. Science Advances 1:1-13.

508 6. Schartup AT, Balcom PH, Soerensen AL, Gosnell KJ, Calder RS, Mason RP, Sunderland
509 EM. 2015. Freshwater discharges drive high levels of methylmercury in Arctic marine
510 biota. Proceedings of the National Academy of Sciences of the United States of America
511 112:11789-94.

512 7. Hsu-Kim H, Kucharzyk KH, Zhang T, Deshusses MA. 2013. Mechanisms regulating
513 mercury bioavailability for methylating microorganisms in the aquatic environment: a
514 critical review. Environmental Science and Technology 47:2441-56.

515 8. Gustin MS, Biester H, Kim CS. 2002. Investigation of the light-enhanced emission of
516 mercury from naturally enriched substrates. Atmospheric Environment 36:3241-3254.
517 9. Amyot M, Lean D, Mierle G. 1997. Photochemical formation of volatile mercury in high
518 Arctic lakes. Environmental Toxicology and Chemistry 16:2054-2063.
519 10. Whalin L, Kim EH, Mason R. 2007. Factors influencing the oxidation, reduction,
520 methylation and demethylation of mercury species in coastal waters. Marine Chemistry
521 107:278-294.
522 11. Poulain AJ, Amyot M, Findlay D, Findlay S, Telor S, Barkay T, Hintelmann H, Amyot
523 M, Findlay D. 2011. Biological and photochemical production of dissolved gaseous
524 mercury in a boreal lake. Limnology 49:2265-2275.
525 12. Carpi A, Lindberg SE. 1997. Sunlight-mediated emission of elemental mercury from soil
526 amended with municipal sewage sludge. Environmental Science and Technology
527 31:2085-2091.
528 13. Vandal GM, Fitzgerald WF, Rolfhus KR, Lamborg CH. 1995. Modeling the elemental
529 mercury cycle in Pallette Lake, Wisconsin, USA. Water, air, and soil pollution 80:529-
530 538.
531 14. Zhang H, Lindberg SE. 2001. Sunlight and iron(III)-induced photochemical production
532 of dissolved gaseous mercury in freshwater. Environmental Science and Technology
533 35:928-935.
534 15. Zhang H. 2006. Photochemical redox reactions of mercury, p 37-79. *In* Atwood DA (ed),
535 Recent Developments in Mercury Science, vol 120.

536 16. O'Driscoll NJ, Lean DRS, Loseto LL, Carignan R, Siciliano SD. 2004. Effect of
537 dissolved organic carbon on the photoproduction of dissolved gaseous mercury in lakes:
538 Potential impacts of forestry. Environmental Science and Technology 38:2664-2672.
539 17. Gu B, Bian Y, Miller CL, Dong W, Jiang X, Liang L. 2011. Mercury reduction and
540 complexation by natural organic matter in anoxic environments. Proceedings of the
541 National Academy of Sciences of the United States of America 108:1479-1483.
542 18. Wiatrowski HA, Das S, Kukkadapu R, Ilton ES, Barkay T, Yee N. 2009. Reduction of
543 Hg(II) to Hg(0) by magnetite. Environmental Science and Technology 43:5307-5313.
544 19. Bone SE, Bargar JR, Sposito G. 2014. Mackinawite (FeS) reduces mercury(II) under
545 sulfidic conditions. Environmental Science and Technology 48:10681-10689.
546 20. Wiatrowski HA, Ward PM, Barkay T. 2006. Novel reduction of mercury(II) by mercury-
547 sensitive dissimilatory metal reducing bacteria. Environmental Science and Technology
548 40:6690-6696.
549 21. Lu X, Liu Y, Johs A, Zhao L, Wang T, Yang Z, Lin H, Elias DA, Pierce EM, Liang L,
550 Barkay T, Gu B. 2016. Anaerobic mercury methylation and demethylation by *Geobacter*
551 *bemidjiensis* Bem. Environmental Science and Technology 50:4366-4373.
552 22. Lin H, Morrell-Falvey JL, Rao B, Liang L, Gu B. 2014. Coupled mercury-cell sorption,
553 reduction, and oxidation on methylmercury production by *Geobacter sulfurreducens*
554 PCA. Environmental Science and Technology 48:11969-11976.
555 23. Grégoire DS, Lavoie NC, Poulain AJ. 2018. Heliobacteria reveal fermentation as a key
556 pathway for mercury reduction in anoxic environments. Environmental Science and
557 Technology 52:4145-4153.

24. Grégoire DS, Poulain AJ. 2016. A physiological role for Hg(II) during phototrophic growth. Nature Geoscience 9:121-125.

25. Barkay T, Kritee K, Boyd E, Geesey G. 2010. A thermophilic bacterial origin and subsequent constraints by redox, light and salinity on the evolution of the microbial mercuric reductase. Environmental Microbiology 12:2904-2917.

26. Grégoire DS, Poulain AJ. 2014. A little bit of light goes a long way: the role of phototrophs on mercury cycling. Metallomics 6:396-407.

27. Poulin BA, Aiken GR, Nagy KL, Monceau A, Krabbenhoft DP, Ryan JN. 2016. Mercury transformation and release differs with depth and time in a contaminated riparian soil during simulated flooding. Geochimica Et Cosmochimica Acta 176:118-138.

28. Bouffard A, Amyot M. 2009. Importance of elemental mercury in lake sediments. Chemosphere 74:1098-1103.

29. Grégoire DS, Poulain AJ. 2018. Shining light on recent advances in microbial mercury cycling. FACETS 3:858-879.

30. Blum JD, Sherman LS, Johnson MW. 2014. Mercury isotopes in earth and environmental sciences. Annual Review of Earth and Planetary Sciences 42:249-269.

31. Zheng W, Gilleaudeau GJ, Kah LC, Anbar AD. 2018. Mercury isotope signatures record photic zone euxinia in the Mesoproterozoic ocean. Proceedings of the National Academy of Sciences 115:10594-10599.

32. Bergquist BA, Blum JD. 2007. Mass-dependent and -independent fractionation of Hg isotopes by photoreduction in aquatic systems. Science 318:417-420.

33. Bergquist BA, Blum JD. 2009. The odds and evens of mercury isotopes: Applications of mass-dependent and mass-independent isotope fractionation. Elements 5:353-357.

34. Kritee K, Blum JD, Johnson MW, Bergquist BA, Barkay T. 2007. Mercury stable isotope fractionation during reduction of Hg(II) to Hg(0) by mercury resistant microorganisms. Environmental Science and Technology 41:1889-1895.

35. Kritee K, Barkay T, Blum JD. 2009. Mass dependent stable isotope fractionation of mercury during mer mediated microbial degradation of monomethylmercury. Geochimica et Cosmochimica Acta 73:1285-1296.

36. Kritee K, Blum JD, Barkay T. 2008. Mercury stable isotope fractionation during reduction of Hg(II) by different microbial pathways. Environmental Science and Technology 42:9171-9177.

37. Wang Y, Janssen SE, Schaefer JK, Yee N, Reinfelder JR. 2020. Tracing the uptake of Hg(II) in an iron-reducing bacterium using mercury stable isotopes. Environmental Science & Technology Letters 7:573-578.

38. Rodríguez-González P, Epov VN, Bridou R, Tessier E, Guyoneaud R, Monperrus M, Amouroux D. 2009. Species-specific stable isotope fractionation of mercury during Hg(II) methylation by an anaerobic bacteria (*Desulfobulbus propionicus*) under dark conditions. Environmental Science and Technology 43:9183-9188.

39. Perrot V, Bridou R, Pedrero Z, Guyoneaud R, Monperrus M, Amouroux D. 2015. Identical Hg isotope mass dependent fractionation signature during methylation by sulfate-reducing bacteria in sulfate and sulfate-free environment. Environmental Science and Technology 49:1365-1373.

40. Janssen SE, Schaefer JK, Barkay T, Reinfelder JR. 2016. Fractionation of mercury stable isotopes during microbial methylmercury production by iron- and sulfate-reducing bacteria. Environmental Science and Technology 50:8077-8083.

41. Kritee K, Motta LC, Blum JD, Tsui MT-K, Reinfelder JR. 2018. Photomicrobial visible light-induced magnetic mass independent fractionation of mercury in a marine microalga. ACS Earth and Space Chemistry 2:432-440.

42. EPA U. 2002. Method 1631, Revision E: Mercury in water by oxidation, purge and trap, and cold vapor atomic fluorescence spectrometry. US Environmental Protection Agency Washington, DC.

43. Janssen SE, Lepak RF, Tate MT, Ogorek JM, DeWild JF, Babiarz CL, Hurley JP, Krabbenhoft DP. 2019. Rapid pre-concentration of mercury in solids and water for isotopic analysis. Analytica Chimica Acta 1054:95-103.

44. Yin R, Krabbenhoft DP, Bergquist BA, Zheng W, Lepak RF, Hurley JP. 2016. Effects of mercury and thallium concentrations on high precision determination of mercury isotopic composition by Neptune Plus multiple collector inductively coupled plasma mass spectrometry. Journal of Analytical Atomic Spectrometry 31:2060-2068.

45. Blum JD, Bergquist BA. 2007. Reporting of variations in the natural isotopic composition of mercury. Analytical and Bioanalytical Chemistry 388:353-359.

46. Lepak RF, Yin R, Krabbenhoft DP, Ogorek JM, DeWild JF, Holsen TM, Hurley JP. 2015. Use of stable isotope signatures to determine mercury sources in the Great Lakes. Environmental Science & Technology Letters 2:335-341.

47. Tang KH, Feng XY, Zhuang WQ, Alvarez-Cohen L, Blankenship RE, Tang YJ. 2010. Carbon flow of Heliobacteria is related more to Clostridia than to the Green Sulfur Bacteria. Journal of Biological Chemistry 285:35104-35112.

625 48. Colombo MJ, Ha J, Reinfelder JR, Barkay T, Yee N. 2013. Anaerobic oxidation of Hg(0)
626 and methylmercury formation by *Desulfovibrio desulfuricans* ND132. Geochimica et
627 Cosmochimica Acta 112:166-177.
628 49. Colombo MJ, Ha J, Reinfelder JR, Barkay T, Yee N. 2014. Oxidation of Hg(0) to Hg(II)
629 by diverse anaerobic bacteria. Chemical Geology 363:334-340.
630 50. Lavoie NC, Grégoire DS, Stenzler BR, Poulain AJ. 2020. Reduced sulphur sources
631 favour Hg(II) reduction during anoxygenic photosynthesis by Heliobacteria. Geobiology
632 18:70-79.
633 51. Icopini GA, Anbar AD, Ruebush SS, Tien M, Brantley SL. 2004. Iron isotope
634 fractionation during microbial reduction of iron: The importance of adsorption. Geology
635 32:205-208.
636 52. Zheng W, Demers JD, Lu X, Bergquist BA, Anbar AD, Blum JD, Gu B. 2019. Mercury
637 stable isotope fractionation during abiotic dark oxidation in the presence of thiols and
638 natural organic matter. Environmental Science and Technology 53:1853-1862.
639 53. Kritee K, Blum JD, Reinfelder JR, Barkay T. 2013. Microbial stable isotope fractionation
640 of mercury: A synthesis of present understanding and future directions. Chemical
641 Geology 336:13-25.
642 54. Tang KH, Yue H, Blankenship RE. 2010. Energy metabolism of *Heliobacterium*
643 *modesticaldum* during phototrophic and chemotrophic growth. Bmc Microbiology 10:150
644 55. Baker PL, Orf GS, Kevershan K, Pyne ME, Bicer T, Redding KE. 2019. Using the
645 endogenous CRISPR-Cas system of *Heliobacterium modesticaldum* to delete the
646 photochemical reaction center core subunit gene. Applied and Environmental
647 Microbiology 85:e01644-19.

648 56. Stenzler B, Hinz A, Ruuskanen M, Poulain AJ. 2017. Ionic strength differentially affects
649 the bioavailability of neutral and negatively charged inorganic Hg complexes.
650 Environmental Science and Technology 51:9653-9662.
651 57. Schaefer JK, Szczuka A, Morel FM. 2014. Effect of divalent metals on Hg(II) uptake and
652 methylation by bacteria. Environmental Science and Technology 48:3007-13.
653 58. Ruuskanen MO, Aris-Brosou S, Poulain AJ. 2020. Swift evolutionary response of
654 microbes to a rise in anthropogenic mercury in the Northern Hemisphere. The ISME
655 Journal 14:788-800.

656

657

658 **FIGURE CAPTIONS**

659 **Figure 1: Total Hg and cumulative Hg^0 production by *H. modesticaldum* grown**
660 **phototrophically and chemotrophically. A, D** THg for live cells and sterile controls without
661 cells. **B, E** Cumulative Hg^0 production for live cells and sterile controls without cells. **C, F**
662 Microbial growth as measured by O.D. 600 nm for live cells and sterile controls without cells. 10
663 nM Hg was supplied in all experiments from the same stock (NIST 3133).

664

665 **Figure 2: Mass dependent fractionation of ^{202}Hg in Hg^{II} (A, C) and Hg^0 (B, D) during**
666 **phototrophic and chemotrophic growth of *H. modesticaldum* and no cell controls**. $\delta^{202}Hg$
667 values for Hg^{II} and Hg^0 are plotted with respect to the fraction of remaining total inorganic Hg^{II}
668 in the bioreactor. Insufficient Hg^0 was recovered from the no cell controls and thus no results are
669 displayed. 10 nM Hg was used in all experiments and Hg was supplied from the same stock
670 (NIST 3133).

671

672 **Figure 3: Compilation of isotopic enrichment factors (ε) for abiotic and biotic Hg**
673 **transformations.** Hg transformations are denoted by different shapes and specific metabolic and
674 chemical pathways have been colour coded. Error bars denote 2 standard deviations for studies
675 where this data was available. In the event that data was presented as a standard error, standard
676 deviation was calculated based on the sample size indicated in each study. Abbreviations on the
677 y-axis denote the following: UV (ultraviolet light), DOC (dissolved organic carbon), AP
678 (anoxygenic photosynthesis), ΔhgcAB (no *hgcAB* gene cluster), and FM (fermentation). The
679 grey-shading in this figure represents light and oxygen. Lighter regions represent habitats where
680 light and oxygen are present and darker regions represent where they are not. The values in this

figure were obtained from the following studies: abiotic dark oxidation (52); abiotic photoreduction (32, 41); aerobic MerA reduction (34, 36); anaerobic respiratory methylation (40); anaerobic respiratory reduction (36, 37); anoxygenic photosynthetic reduction (this study); fermentative reduction (this study); oxygenic photosynthetic reduction (41). The raw data in this figure are in **Table S5**.

SUPPORTING INFORMATION CAPTIONS

Figure S1: Schematic of the bioreactor setup used to measure Hg stable isotope fractionation for Hg^{II} and Hg^{0} during the anaerobic reduction of Hg^{II}.

Figure S2: **Total Hg mass balance for isotope fractionation experiments under phototrophic and chemotrophic growth conditions.** The average recovery across all experiments was 94.40 ± 9.50 % (n=7) and is shown by the dashed red line.

Figure S3: Mass dependent fractionation of $^{202}Hg^{II}$ in phototrophically (A, B) and chemotrophically (C, D) grown *H. modesticaldum*. $\delta^{202}Hg$ values for Hg^{II} are plotted as open system Rayleigh fractionation models with $\ln(R/R_0)$ vs $\ln(f_r)$. The amount of Hg^{II} remaining in the reactor was used to calculate f_r (see Methods). The 0h time point for chemotrophic live cells replicate #1 was omitted from the regression fitted to the data for Hg^{II} (C) as this suggested an alternative process was contributing to isotopic fractionation earlier on in the experiment.

702 **Figure S4: Mass dependent fractionation of $^{202}Hg^0$ in phototrophically (A, B) and**
703 **chemotrophically (C, D) grown *H. modesticaldum*.** δ^{202}Hg values for Hg^0 are plotted as open
704 system Rayleigh fractionation models with $\ln(R/R_0)$ vs $\ln(f_r)$. The amount of Hg^{II} remaining in
705 the reactor was used to calculate f_r (see Methods). The 3h time point for phototrophic cells in
706 replicates #1 and 2 were omitted from the regression fitted to the data for Hg^0 (A, B) as this
707 suggested an alternative process was contributing to isotopic fractionation earlier on in the
708 experiment. No significant regressions were obtained for chemotrophic cells and as such no
709 models are presented.
710
711 **Table S1**: Total Hg concentrations and Hg isotope ratios for the reactant pool Hg^{II} in
712 phototrophic and chemotrophic growth conditions experiments. Each line corresponds to an
713 individual sample and technical duplicates were taken for each time point. Std represents the
714 standard deviation from analytical replicates on the MC-ICP-MS. Abbreviations denote Metabo.
715 = Metabolism; Photo. = Phototrophy; Chemo. = Chemotrophy; Treat. = Treatment; Hg conc. =
716 Hg concentration, rep = replicate; Avg = average; Std = Standard deviation; ctl = control, MED
717 = medium. δ^{202}Hg values in **bold** denote those that deviate substantially from the composition of
718 the NIST 3133 standard in medium spiked controls.
719
720 **Table S2:** Total Hg concentrations and Hg isotope ratios for the Hg^0 pool in phototrophic and
721 chemotrophic growth conditions experiments. Each line corresponds to the Hg present on two
722 gold traps used to sample each time point in parallel. Std represents the standard deviation from
723 analytical replicates on the MC-ICP-MS. Abbreviations denote the following: Metabo. =

Metabolism; Photo. = Phototrophy; Chemo. = Chemotrophy; Treat. = Treatment; Hg conc. = Hg concentration, rep = replicate; Avg = average; Std = Standard deviation.

Table S3: Summary of regression models for mass dependent fractionation of $^{202}Hg^{II}$ and $^{202}Hg^{0}$ in phototrophically and chemotrophically grown *H. modesticaldum* cultures. P-values for regressions that displayed a significant ($p<0.05$) fit are shown in **bold.**

Table S4: Comparison of measured and calculated isotope fractionation values for the reactant pool of Hg^{II} using a mass balance approach. Measured values of Hg concentration and $\delta^{202}Hg$ are represented as an average of replicates from experiments presented in Tables S1 and S3. Predicted values for media were obtained using the equations outlined for mass balance calculations. Differences between the measured and predicted values that are substantially greater than the analytical variability of measurements (2SD = 0.08) are shown in **bold**. Abbreviations denote Photo. = phototrophic, Chemo. = chemotrophic, rep = replicates, Avg. = average, Pred. = predicted.

Table S5: Comparison of enrichment factors and measures of variability used in this study and the original cited work. Values in bold represent calculation ratios that differ between the original article cited and the current study. Abbreviations: SD = standard deviation, SE = standard error, p = product, r = reactant, Ox. = oxygenic, Anox. = anoxygenic, PS = photosynthesis.